Scalable High-Power Redox Capacitors with Aligned Nanoforests of Crystalline MnO_2 Nanorods by High Voltage Electrophoretic Deposition

Sunand Santhanagopalan, Anirudh Balram, and Dennis Desheng Meng*

Multi-Scale Energy Systems (MuSES) Laboratory, Department of Mechanical Engineering - Engineering Mechanics, Michigan Technological University, Houghton, Michigan 49931, United States

ABSTRACT

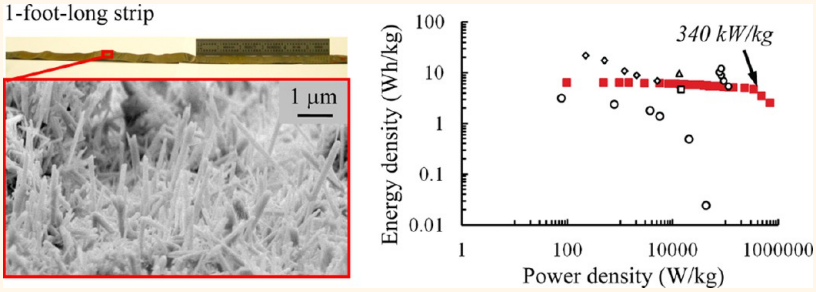

It is commonly perceived that reduction—oxidation (redox) capacitors have to sacrifice power density to achieve higher energy density than carbon-based electric double layer capacitors. In this work, we report the synergetic advantages of combining the high crystallinity of hydrothermally synthesized α-MnO_2 nanorods with alignment for high performance redox capacitors. Such an approach is enabled by high voltage electrophoretic deposition (HVEPD) technology which can obtain vertically aligned nanoforests with great process versatility. The scalable nanomanufacturing process is demonstrated by roll-printing an aligned forest of α-MnO_2 nanorods on a large flexible substrate (1 inch by 1 foot). The electrodes show very high power density (340 kW/kg at an energy density of 4.7 Wh/kg) and excellent cyclability (over 92% capacitance retention over 2000 cycles). Pretreatment of the substrate and use of a conductive holding layer have also been shown to significantly reduce the contact resistance between the aligned nanoforests and the substrates. High areal specific capacitances of around 8500 $\mu F/cm^2$ have been obtained for each electrode with a two-electrode device configuration. Over 93% capacitance retention was observed when the cycling current densities were increased from 0.25 to 10 mA/cm^2, indicating high rate capabilities of the fabricated electrodes and resulting in the very high attainable power density. The high performance of the electrodes is attributed to the crystallographic structure, 1D morphology, aligned orientation, and low contact resistance.

KEYWORDS: electrophoretic deposition · high power supercapacitors · scalable nanomanufacturing · aligned nanoforests

Supercapacitors are promising energy storage devices, especially surge power providers, in a broad range of applications, including energy harvesters, microelectromechanical systems (MEMS), portable electronics, electric vehicles, and high-performance, hybrid power sources by coupling with batteries.[1−4] They have garnered interest due to their high power density, quick charging, long cycling life, and great reversibility.[5−7] Supercapacitors based on different electrode materials store/deliver energy with different working principles. Carbon materials are used extensively for electric double layer capacitors (EDLC) where charge is stored by nonfaradaic surface interactions.[8−10] On the other hand, conductive polymers[11,12] and various transition metal oxides[13−18] are used for reduction—oxidation (redox) capacitors where faradaic reactions can be employed to improve charge/energy storage capability, while typically compromising the charge/discharge rate, power density, and cyclability to a certain degree.[19]

Among the transition metal oxides, manganese dioxide (MnO_2) is especially attractive due to its low cost, environmental friendliness, abundance in nature and relatively

* Address correspondence to dmeng@mtu.edu.

Received for review September 25, 2012 and accepted January 31, 2013.

Published online February 01, 2013
10.1021/nn3044462

high specific capacitances. Manganese dioxide exists in different crystallographic structures owing to the different ways the MnO_6 octahedra are interlinked, that result in various tunnel sizes. These tunnels allow for foreign cations to be stored within them, while enabling the conversion of Mn^{4+} ions to Mn^{3+} ions for charge balance.[20] The quantity of cations that can be stored depends on the size of these tunnels. Among the different MnO_2 structures, α-MnO_2 with 2×2 tunnels formed from double chains of MnO_6 has one of the largest tunnel sizes.[20−22] As a result, α-MnO_2 can store more foreign cations in reversible faradaic reactions, rendering it with the highest specific capacitance among all the known crystal phases of MnO_2.[21]

The performance of a supercapacitor can be strongly affected by the crystallographic structure of active material, as well as other factors like morphology, exposed surface area, electrical contact with current collectors, amount of cations present, *etc.* It is well-known that one-dimensional (1D), nanostructured morphology allows for large surface area, short diffusion paths that enable fast electron/ion transfer, better stress/strain accommodation, and modified electrochemical properties.[23] Ordered architectures with vertically aligned forests of such 1D nanostructures provide additional advantages like greater packing density, ballistic electron transport along the vertical axis, better electrolyte access and better electrical contact that consequently lead to higher rate capabilities and greater cyclic stabilities.[24,25] Aligned forests of CNTs have inspired a few innovative configurations of electrodes and devices, such as interdigitated planar devices,[26] Origami-folded electrodes,[27] and forests of nanoflowers on vertically aligned stems.[28] For example, by integrating aligned CNT nanoforest into a microscale supercapacitor using a novel synthesis process, Jiang et al. achieved an impressive performance improvement by 3 orders of magnitude,[26] indicating the power of alignment and opening the door to new opportunities. Electric-field-induced alignment has been tried for carbon nanotubes or metallic nanoparticles using methods based on electrophoretic deposition (EPD)[29−33] and dielectrophoresis (DEP).[34−37] DEP is limited in its process versatility and scalability due to the required small microfabricated electrode gaps and preferable deposition on electrode edges. EPD, on the other hand, has faced problems like bundle formation, low density, poor alignment, and difficulty in control. In any case, such innovative methods have been tried predominantly for carbon nanotubes and have not yet been used to obtain aligned forests of MnO_2 nanoparticles.

MnO_2 nanostructures have been synthesized by various methods such as coprecipitation, chemical reduction, sol−gel synthesis, thermal decomposition, and electrochemical deposition.[6,38−40] Ordered/aligned MnO_2 nanostructures have also been obtained by sol−gel template synthesis,[41] template-based electrochemical deposition,[42] electrochemical anodization[43] and anodic electrochemical deposition,[44] *etc.* However, it has been challenging to obtain nanomaterial with both optimal crystallographic structure and highly ordered/aligned morphology at the same time. As a result, the performance can deteriorate quickly at high charge/discharge rate and during long cycling even if the nanorods can originally be well aligned, due to the lack of pure crystallographic structures, optimal 1D morphology, and low electrical contact resistance. Furthermore, the use of templates and high temperatures in the above-mentioned methods seriously limits the ability to obtain large flexible electrodes on current-collecting substrates for applications in large-scale supercapacitor devices.

On the other hand, hydrothermal synthesis has been used to produce 1D nanostructures of MnO_2 with superb process control and highly crystalline structures, due to the relatively higher process temperature and pressure.[22,45−48] Improved capacitive behavior of highly crystalline 1D MnO_2 nanostructures by hydrothermal synthesis has been repeatedly observed.[21,49,50] Moreover, the relatively high yields of hydrothermal synthesis made it a good choice for scale-up production. However, hydrothermal synthesis has not been reported to directly produce ordered arrays on conductive substrates that can take the aforementioned advantages and innovative device/electrode configuration of aligned nanoforests.[26−28,51] A versatile, scalable, and facile technique for device fabrication using ordered, high-quality MnO_2 nanostructures is yet to be realized, together with the demand on process compatibility (*e.g.*, with flexible substrates and Si-microfabrication processes).

In this work, we propose to first obtain highly crystalline α-MnO_2 nanorods by low-cost, scalable hydrothermal synthesis method, and then align/deposit them by our previously reported post synthesis method named high voltage electrophoretic deposition (HVEPD).[52] Electrophoretic deposition (EPD) is a process in which DC voltage is used to move charged particles in a stable dispersion toward the oppositely charged electrode. As a result, the particles are deposited on the electrode surface due to surface interactions.[53] HVEPD enables great flexibility on the choice of material (*e.g.*, CNTs and various types of MnO_2) and substrates (*e.g.*, flexible and transparent). It is also a template-free, room-temperature process with high compatibility to microfabrication. We have previously reported aligned nanoforests of CNT and β-MnO_2 nanorods using HVEPD and proved that the process is compatible with flexible and transparent electrodes.[52] In this work, we have been able to show the full advantages of combining hydrothermal synthesis and HVEPD which turns out to enable supercapacitor electrodes with excellent retention of capacitance over high current density and long cycling. Furthermore, the prospect of durable, high-power supercapacitors on roll-printed large flexible substrates

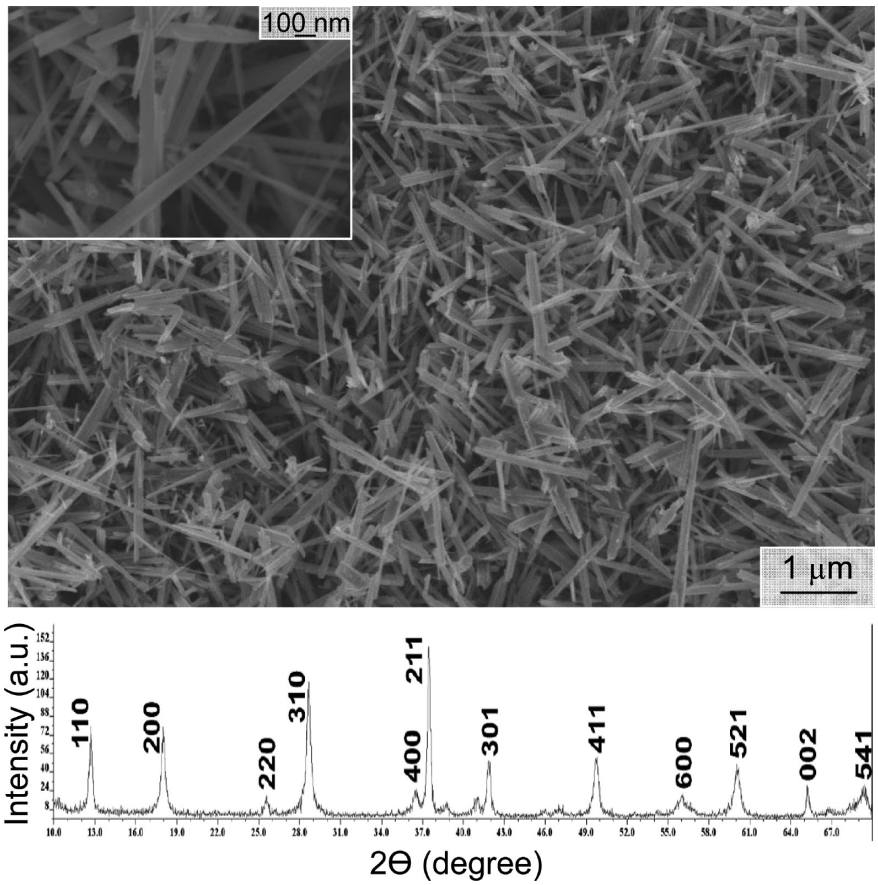

Figure 1. FESEM image and XRD analysis of α-MnO_2 nanorods synthesized by hydrothermal synthesis.

has been demonstrated by verifying that such scale-up leads to no performance deterioration. The high performance in this work has been attributed to the optimal crystallographic structures of the hydrothermal α-MnO_2 nanorods, the alignment parameters optimized for the nanorods, the conductive holding layer and the pretreated substrate to remove any existing oxide layer. The work has provided a unique opportunity to look at MnO_2-based redox capacitors from the perspectives of not only material but also device configuration and electrode morphology.

RESULTS AND DISCUSSIONS

Hydrothermal Synthesis of α-MnO_2 Nanorods. Crystalline α-MnO_2 nanorods were first synthesized using a facile hydrothermal synthesis technique.[54] $KMnO_4$ was used to oxidize $MnSO_4$ under hydrothermal conditions and produce uniform nanorods. An optimal ratio of the reactants was adopted to obtain the desired morphology and crystallographic structure. It is believed that the formation of the α-MnO_2 nanorods is through the transformation of initially formed δ-MnO_2 phase during hydrothermal process.[54] The as-produced α-MnO_2 nanorods were characterized using the field emission scanning microscopy (FESEM) and by X-ray diffraction analysis (XRD) (Figure 1). The nanorods appeared fairly uniform with a length of 2−6 μm and diameter of about 20−80 nm. XRD peaks were indexed by comparison to literature[54,55] and JCPDS 44−141, which confirms the crystalline structure of the synthesized nanorods as α-MnO_2. The sharp peaks in the XRD analysis indicate high crystallinity of the synthesized material.

High Voltage Electrophoretic Deposition. HVEPD was used to obtain aligned forests of as-synthesized α-MnO_2 nanorods. The method relies on using a relatively high voltage (*i.e.*, strong electric field) to align the nanorods along the electric field, maintaining a low concentration dispersion to avoid bundle formation during deposition and simultaneous deposition of a holding layer to maintain the aligned orientation. Figure 2 shows the working mechanism of the HVEPD process with the schematic of the continuous roll-printing HVEPD setup. α-MnO_2 nanorods were dispersed in isopropyl alcohol (IPA) with a precursor salt for the holding layer also being dissolved. A nonaqueous dispersion system was chosen to eliminate bubble formation during deposition caused by water electrolysis. With its optimal concentration, the precursor salt fulfills two functions: ions in the solvent are adsorbed onto the surface of nanoparticles to stabilize them and facilitate their deposition,[53] while excess ions get reduced and deposit as the holding layer during HVEPD.[52] During deposition, the charged nanorods are moved through the dispersion by using a certain

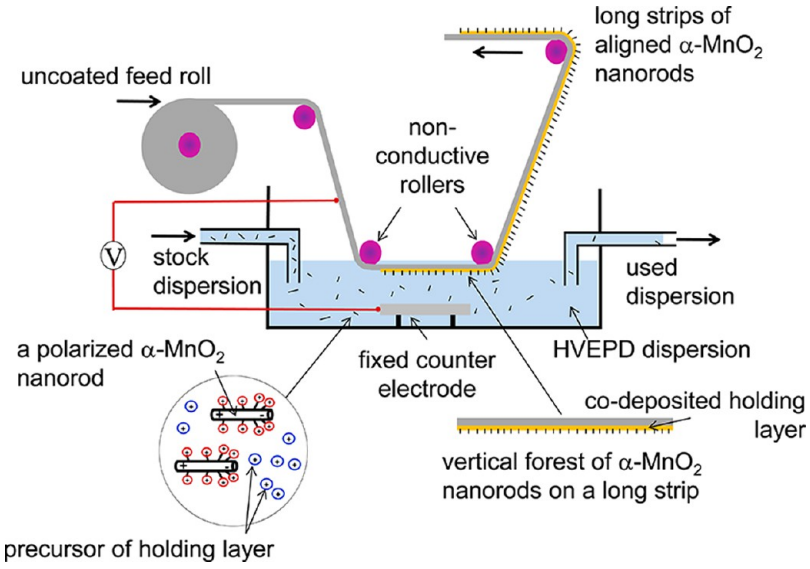

Figure 2. Schematic and working mechanism of continuous HVEPD setup.

voltage, which, if high enough, would polarize the nanorods to overcome Brownian motion and align them along the electric field.[56,57] However, the polarized nanorods generally tend to attract oppositely charged ends and aggregate during deposition.[58] To limit such aggregation, relatively low concentration of the nanorods has been used to obtain densely aligned nanoforests.[52] The time of deposition can also be controlled to avoid over deposition or crowding.

Control experiments were carried out to find the optimal parameters needed to align the as-synthesized α-MnO_2 nanorods. Alignment was first achieved with a nonconductive $Mg(OH)_2$ holding layer by using a Mg precursor salt. Good alignment was obtained at a deposition voltage of 800 V and time of 30 s. The concentration of α-MnO_2 nanorods was maintained at 0.01 mg/mL and that of the Mg precursor salt was kept at 0.005 mg/mL. In order to improve the electrical contact between the nanorods and the rigid stainless steel (SS) substrates, a conductive Ni holding layer has also been employed in this work. A Ni salt was used as the precursor with a concentration of 0.0075 mg/mL, while the nanorod concentration was kept at 0.01 mg/mL. It has been noticed that the amount of ions adsorbed on the nanorod surface, ionic mobility and the optimal amount of ions in the dispersion vary with the type of precursor salts. The salt concentrations have to be adjusted to provide enough charge on the nanorods and deposit a sufficiently thick holding layer. On the other hand, an excess of precursor salt may lead to unstable dispersion, deteriorated alignment, and reduced specific capacitance due to excess Ni content. The deposition voltage and time for optimal alignment (determined by FESEM observation and electrochemical testing) were found to be 800 V and 30 s respectively, same as the values for HVEPD with Mg salt as the precursor. Figure 3 shows the tilted side views of the aligned nanoforests with the two different holding layers. The observed alignment is in the vertical direction relative to the substrate as opposed to a random or horizontally aligned network. It has been shown in our previously published work that such vertically aligned nanoforests could not be achieved using drop casting or EPD with lower voltage.[52,59] The alignment on the vertical direction, although not perfect, has previously been quantitatively revealed by their improved electrochemical performance, higher contact angle (to superhydrophobicity) after applying polymer coating, and capability to electrically connect two separated electrodes over a larger distance.[52] There is certainly room for further improvement in the quality of alignment. The vertically aligned nanoforests prepared by HVEPD lead to increased surface area and reduced contact resistance that enable the high electrochemical performance, as to be outlined in this paper. Dense nanoforests of α-MnO_2 nanorods could be achieved using both the precursor salts. However, it is observed that the alignment and uniformity have been slightly improved in the samples with a Ni holding layer. It can be attributed to the avoidance of electric field distortion by the patchy, nonconductive $Mg(OH)_2$ holding layer in the former case.

To further improve the electrical contact, the SS substrates were pretreated to remove any existing oxide layer on the surface. A standard Wood's strike[60] was used to remove the oxide layer and deposit a thin layer of Ni on the surface of the SS substrate. The Wood's strike is commonly used in electroplating applications to improve mechanical adhesion.[60] In this case, the Wood's strike was used to provide better electrical contact between the nanorods and the substrate while improving the adhesion. HVEPD was then conducted on the pretreated substrate to obtain aligned nanoforests with low contact resistance.

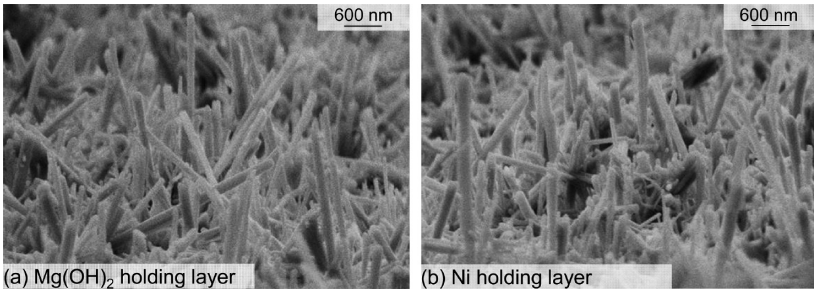

Figure 3. FESEM images of aligned nanoforests of α-MnO_2 nanorods with different holding layers.

Electrochemical Characterization. The effect of improved electrical contact on the electrochemical performance was studied using a two-electrode Swagelok cell. Testing with a two-electrode setup represents the scenario of a practical, packaged cell.[61] Three types of samples were prepared, characterized, and compared, as shown in Table 1.

Galvanostatic charge−discharge was carried out to find the specific capacitance for the three samples. Figure 4a shows the typical charge−discharge curves measured at a constant current density of 0.25 mA/cm^2. The IR drop, as defined as the drop in voltage at the point of current switching, is indicative of the contact resistance of the sample. The capacitance values were calculated using the linear part of the discharge curve after the IR drop (Table 2). The total areal specific capacitance of the complete two-electrode system was calculated using the relation given below

$$C_A = C/A = (I \times dt)/(dv \times A) \quad (1)$$

,where C is the total measured capacitance of the two-electrode system; I is the constant current used during discharge; dt is the discharge time from the near linear part of the discharge curve after the IR drop; dv is the voltage difference during time dt and A is the area of a single electrode.

As compared with samples II and III, the use of a conductive holding layer and pretreated substrate in sample I has led to greatly reduced IR drop which indicates a lower contact resistance. It is well-known that reduced contact resistance helps improve electrochemical capacitance.[8] The impact of improved contact is seen by a roughly 2-fold increase in the capacitance values. This effect is also seen in the cyclic voltammetry (CV) curves shown in Supporting Information S1, which shows no distortion in the near-rectangle shape at high scan rates. As a result, the stability of the sample during high rate cycling has opened up its great potential for high power applications to be demonstrated later in this work. Supporting Information S2 shows the Nyquist plots for the three samples taken by electrochemical impedance spectroscopy (EIS). The EIS data agrees well with the conclusion drawn from IR drop that sample I has the lowest contact resistance.

The high rate capability of these samples was checked by characterizing at different current densities. Figure 4b shows the variation of C_A (the areal specific capacitance) in response to ~40 times increase in the current density, from 0.25 mA/cm^2 up to 10 mA/cm^2. The highest retention in C_A was seen for sample I, which retained over 93% of its original value. In comparison, samples II and III were able to retain around 88 and 78% of their original C_A values, respectively. High rate capability of the reported samples, especially sample I, is attributed to the crystallographic structure of the nanomaterials used which allows for faster intercalation/deintercalation of ions. It is known that the material utilization in a pseudocapacitor decrease with faster charge/discharge as the speed of intercalation/deintercalation may not be able to keep up with the speed of the current. Thus, at high current densities the charge storage phenomena becomes more of a surface phenomenon than redox reactions.[46] A well-aligned crystalline nanoforest with good electrical contact allows for higher rates of intercalation/deintercalation, better electrolyte access to the material and faster ion/electron transport through the current collector. This allows for better capacitance retention as well as low contact resistance that enable high power performance. It has also been reported that the rate capabilities of MnO_2 improves when doped by certain materials[62,63] or when combined with conductive materials in the deposit.[64] In case of samples I and II, Ni ions get adsorbed and deposited over the nanorod surface which may also have contributed to the improvement of the high rate stability of the electrode. To confirm this, the nanorods were removed from the HVEPD substrate to check for Ni present on the surface of nanorods while avoiding the interference from the Ni in the holding layer. The presence of Ni on the nanorods was revealed using EDX mapping, which shows mostly overlapping distribution patterns for O, Mn, and Ni elements. (see Supporting Information S3).

TABLE 1. Three Types of Samples Fabricated and Characterized

Sample I	aligned α-MnO_2 nanorods on pretreated SS substrate with Ni holding layer
Sample II	aligned α-MnO_2 nanorods on untreated SS substrate with Ni holding layer
Sample III	aligned α-MnO_2 nanorods on untreated SS substrates with $Mg(OH)_2$ holding layer

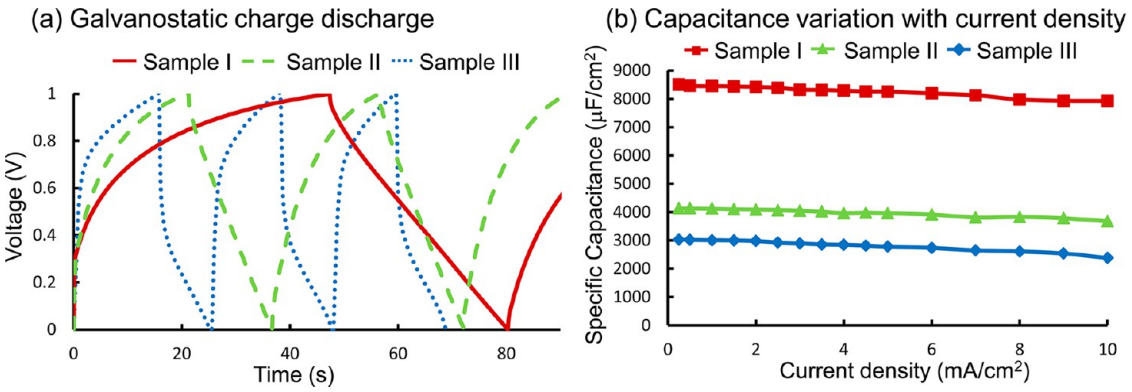

Figure 4. (a) Galvanostatic charge discharge curves at 0.25 mA/cm^2 current for the three types of samples defined in Table 1 and (b) variation of device capacitance with increasing current density for sample I showing high rate stability.

TABLE 2. IR Drop and Capacitance Values for the Three Types of Samples Defined in Table 1

	IR drop (V)	areal specific capacitance (μF/cm^2)
Sample I	0.03	8501
Sample II	0.11	4140
Sample III	0.40	3023

Another important factor in gauging the performance of a supercapacitor electrode is its cycle life. Although EDLCs are known for their excellent durability, substantial loss of capacitance during long cycling is common with redox capacitors. The main degradation mechanisms considered for such capacitance fading are the loss of material during cycling and deteriorating contact between with the current collector.[21,65] Physiochemical feature evolution of the material during cycling may also cause significant loss of capacitance.[44,65] In the reported approach, nanocrystalline structures allow for better structural accommodation with more free space allowance for stress relief during ion intercalation/deintercalation. The tendency for lattice structure distortion or morphology change during long-term cycling would thus be less in highly crystalline nanomaterials.[44] At the same time, well-aligned nanoforests and good electrical contact allow for better electrolyte access, little deterioration of contact due to better stress accommodation on the tiny end of nanorods, and less loss of material. As a result, the loss of capacitance over cycling has been dramatically reduced as compared to previously reported for similar nano-MnO_2 systems, which is typically 70−85% over 1000 cycles.[66] For example, 69.0% retention over 1000 cycles has been reported for nano-MnO_2 system, which was improved to 84.1% by incorporating graphene oxide.[67] Figure 5 shows the capacitance fading over 2000 cycles for the three samples. Samples II and III are able to retain about 87 and 81% of their original capacitance. Sample I on the other hand shows excellent capacitance retention of over 92%. The results have confirmed that the cycle

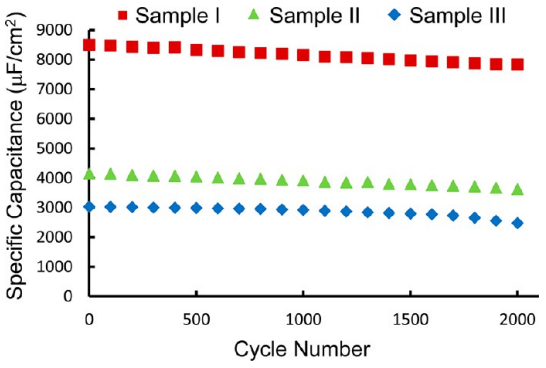

Figure 5. Drop of device capacitance over 2000 cycles for the three types of samples defined in Table 1.

stability of a redox capacitor can be dramatically improved by synergistically combining highly crystallinity of hydrothermal nanorods with alignment and reduction of contact resistance. At the same time, the results also indicate good adhesion between the nanoforests and the substrate.

High rate capability of the aligned α-MnO_2 nanoforests achieved with sample I implies its great potential for high power applications. The power and energy densities for the three samples were calculated according to the following relations:

$$P_D = IV/2m; \quad (2)$$

$$E_D = CV^2/2(2m) \quad (3)$$

.Here I is the constant current at which galvanostatic charge−discharge cycles were run; V is the voltage drop in the near-linear portion of the discharge curve after the IR drop (i.e., attainable cell voltage); m is the mass of active material on one electrode and C is the total capacitance measured from the two-electrode system. The power and energy densities are correlated with each other in the Ragone plots as Figure 6 shows, where each data point is calculated from the capacitance and voltage values from a particular discharge current. It is important to note that as the cycling rate

(current during cycling) changes, the IR drop tends to change accordingly, leading to a different attainable cell voltage V for the calculation of attainable power density and the corresponding energy density at a particular discharge current. Generally speaking, good rate capability with high capacitance and low contact resistance can enable high power characteristics. The Ragone plots of all three types of samples are shown in Figure 6. Sample I shows an impressive trait to offer high power density without significantly sacrificing its energy density. Particularly, when the power density was increased by ~3500 times from 97 W/kg to 340 kW/kg, the energy density only dropped by ~27% from 6.5 Wh/kg to 4.7 Wh/kg. As a result, well-balanced performance on power and energy can be achieved.

For example, to take the high power density before a significant drop in energy density occurs, sample I can achieve a power density of 340 kW/kg with an energy density of 4.7 Wh/kg. In comparison, samples II and III achieved power density of around 104 and 61 kW/kg respectively before severe drop of energy density happens. Such high performance of sample I is a direct result of its capability to retain high attainable cell voltage. For reference, the Ragone plot is also marked with a few examples of the highest performance achieved with MnO_2 nanostructures and their composites in the most recent literature.[66,68−70] It is noticed that the 340 kW/kg attainable power density obtained in this work is about 3 times of that reported in ref 66 and more than 1 order of magnitude higher than the typical values with MnO_2-based systems.[68−70] The power density achieved in this work is also significantly higher than that of a typical CNT-based EDLC.[71] The excellent high-power performance can be again attributed to the combination of highly crystalline redox material, 1D morphology, well aligned dense nanoforests, and good electrical contact, especially in sample I.

It should be noted that higher power density can be obtained with hydrous ruthenium oxide (e.g., 1100 kW/kg at 76.4 Wh/kg).[72] However, the toxicity and high cost of the latter may seriously limit its practical applications. It is also interesting to note that the performance of the α-MnO_2 nanorods may be significantly affected by their length, which is currently 2−6 μm in this study. With an increasing length of the nanorods, a larger surface area may be available for energy storage. Meanwhile, the increased resistance and decreased material utilization may negatively impact the energy and power density. An in-depth study may be able to yield an optimum length at which maximum specific capacitance, energy density, and/or power density can be obtained. This may be explored in future work. Nevertheless, the HVEPD technique allows great flexibility on material and substrate selection. The reported approach can thus enable the

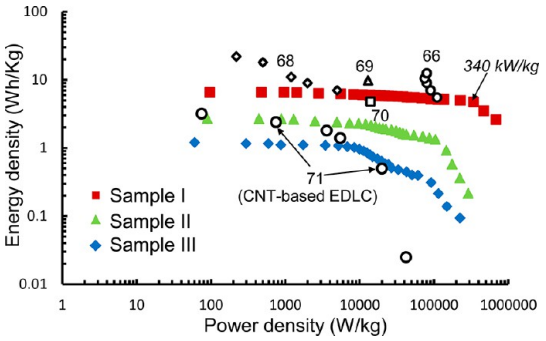

Figure 6. Ragone plot for the three types of samples defined in Table 1, as compared with a few examples of the highest performance achieved with MnO_2 nanostructures and their composites in the most recent literature. The 340 kW/kg attainable power density obtained in this work is about 3 times of that reported in ref 66 and more than 1 order of magnitude higher than the typical values with MnO_2-based systems.[68−70] The power density achieved is also significantly higher than that of a typical CNT-based EDLC.[71]

fabrication of aligned forests of many high capacitance 1D nanomaterials, including ruthenium oxide nanorods or nanotubes of different sizes, on highly conductive substrates.

Continuous HVEPD. In many practical applications, such as electrical vehicles, the size of capacitors needs to be significantly larger than typical lab-scale devices, to provide enough total power and energy.[73,74] The HVEPD approach demonstrated in this work allows for scaling up the electrodes to much larger substrates, due to its mild deposition condition and robust process. Moreover, the orientation control makes the reported approach stand out among existing electrode preparation methods that might be scalable or applicable to flexible substrates, such as rod coating or pasting nanomaterials.[75] To demonstrate such scalability, a continuous HVEPD setup, as illustrated in Figure 2, was built to achieve aligned nanoforests on long strips of flexible SS sheets. The flexible SS sheet was mounted on nonconductive rollers and run through the HVEPD dispersion using a DC motor. To achieve a well-aligned nanoforest all through the long substrate, it was important to control three key factors, namely feed speed of substrate, constant concentration of the dispersion and moderate dispersion agitation to ensure uniformity of the dispersion while avoiding disturbance on alignment of the nanorods. The feed speed of flexible SS substrate, together with its total length that is immersed in the dispersion, determines the time of deposition, which should match the optimal deposition time found on the rigid small substrate (30 s in this case). The total area on which deposition occurs also depends on the width of the strip being used. This width, together with its length immersed in the dispersion, thus determines the total areal speed of deposition for a large-scale production process. A 1 in. wide strip was used in this

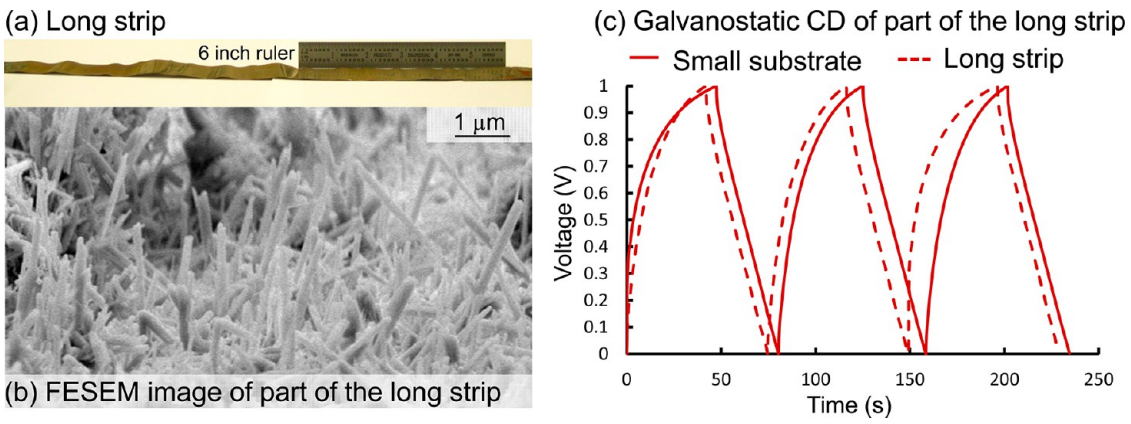

Figure 7. (a) Aligned nanoforests of α-MnO_2 nanorods deposited on a long flexible strip. (b) FESEM image of part of the long strip. (c) Galvanostatic charge discharge curves of part of the long strip compared to the small rigid substrate.

case, thus a total areal deposition speed of 2 $in.^2$/min or 5.08 cm^2/min was achieved. The speed of deposition can be increased further by using a larger deposition container. For future commercialization, the deposition speed can be benchmarked against that of commercial batteries and capacitors. As deposition occurs on the long moving strip, the α-MnO_2 nanorods and Ni^{2+} ions in the HVEPD dispersion get depleted. A multichannel pump was used to continuously replenish the dispersion while keeping the volume constant. A stock dispersion with a higher concentration was used to replenish the HVEPD dispersion. The concentration of α-MnO_2 nanorods and Ni precursor salt in the stock dispersion was calculated using a simple mass balance:

$$\text{Mass in deposit} + \text{Mass being pumped out} = \text{Mass required to be pumped in.} \quad (5)$$

During replenishment, the incoming/outgoing fluid flow may agitate the dispersion and thus affect the disposition. Fortunately, under laminar conditions the fluid flow would not cause a torque on the nanorods but only a constant drag force.[76] The alignment will thus not be affected. However, if the nanorods experience significant random motion due to turbulent disturbance, the electric field required to align them would have to be increased to overcome that motion. To avoid such effect, the speed at which the HVEPD dispersion is replenished was controlled to avoid turbulent disturbance of the HVEPD dispersion. This speed was maintained constant by running the pump at a rate of 8 mL/min. Considering the flow between parallel plates as a plane Couette flow, the maximum Reynold's number (R_e) are calculated to be ~4, far from the turbulent regime R_e >4000. In our previous work,[77] aligned nanoforests of CNTs were achieved on long strips of flexible SS sheets by controlling these key factors at similar range. The quality of nanoforests had been confirmed to be near identical on the large flexible substrate by continuous HVEPD and the small

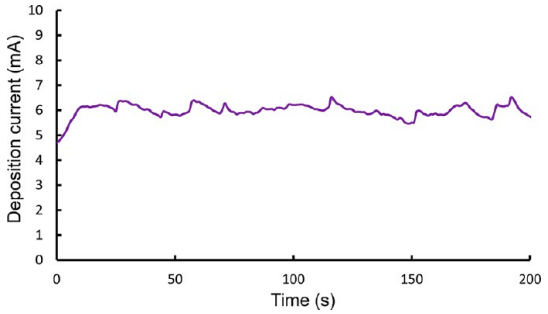

Figure 8. Deposition current during continuous HVEPD.

rigid substrate, providing further evidence that no excess torque would act on the nanomaterials. It is thus expected that the alignment and deposition in this work will also not be significantly disturbed by the flow of dispersion, which will be confirmed in the following paragraph.

Figure 7a shows part of the long strip placed against a 6-in. ruler. The high-quality deposition over the whole strip has been confirmed visually as a uniform mirror-like finish. The FESEM image in Figure 7b shows the alignment of the deposited α-MnO_2 nanorods on a piece cut from the long strip sample. There is no visible deterioration of alignment in the sample obtained by the continuous HVEPD process. Figure 7c shows the galvanostatic charge–discharge curves for parts of the long strip with similar area as a small rigid sample I. It has been tested in a two-electrode setup and evaluated against the galvanostatic charge–discharge curves of sample I. The specific capacitance and IR drop values found for the long strip were 8496.8 $\mu F/cm^2$ and 0.036 V respectively, as compared with 8501.3 $\mu F/cm^2$ and 0.038 V measured in sample I. No substantial deterioration in the electrochemical performance has been observed in the scaled up electrodes. It is thus verified that the continuous HVEPD has the potential to print large-scale electrodes with aligned forests of α-MnO_2 nanorods for various applications, which had been difficult with electrode preparation methods based on templated deposition and many other existing methods.

In this work, the flexible SS sheets were also first pretreated with a continuous Wood's strike. Subsequently, aligned forests of α-MnO_2 nanorods were deposited uniformly on 1-foot-long SS strip using the continuous HVEPD setup. The deposition current during continuous HVEPD is monitored and used as an indicator of uniform deposition over the long strip. Figure 8 shows the deposition current measured over 3 min (the time to deposit on a long strip of about 6 in.) using a digital multimeter connected in series with the continuous HVEPD setup. The current stays pretty constant during the entire deposition process, indicating that the concentration of the HVEPD dispersion is maintained constant. A significant variation in the deposition current would indicate a distortion of deposition, which may be caused by errors such as loss of wire connections, stuck strip, empty tank of stock solution *etc*. With this simple in-process monitoring mechanism, such errors can be immediately recognized and corrected.

CONCLUSIONS

Aligned forests of highly crystalline α-MnO_2 nanorods with excellent electrical contact to the current-collecting substrates have been fabricated by a novel HVEPD process. The effect of improving electrical contact, with a conductive holding layer and pretreated substrate, on the electrochemical performance has been investigated using cyclic voltammetry, galvanostatic charge−discharge and electrochemical impedance spectroscopy. Highly crystalline α-MnO_2 nanorods, well-aligned nanoforests, good electrical contact and strong adhesion have been simultaneously achieved, yielding a high single electrode capacitance of 200 F/g. Excellent capacitance retention of 92% over 2000 cycles has been observed with the fabricated electrodes.

The high rate capability of the electrode was also confirmed by retaining 93% of its original specific capacitance in response to ~40 times increase in the current density, up to 10 mA/cm^2. The high rate capability has led to a high power density of 340 kW/kg at an energy density of 4.7 Wh/kg. The high power density achieved in this work thus provides clear evidence against the common perception that redox capacitors have to sacrifice power density to achieve higher energy density than EDLCs. HVEPD was also shown as a versatile, simple method to achieve such high performance electrodes on a large scale by continuous printing on long strips of flexible electrodes. A simple in-process monitoring mechanism, based on current measurement, can be employed to continuously detect process errors and ensure the process reliability. Large-scale electrodes produced by continuous HVEPD have been shown to have consistent electrochemical performance as the small rigid samples. The excellent scalability has made the reported approach very promising in practical applications of various cell sizes.

METHODS

Chemicals. All the chemicals used in the experiments were analytical grade and used as purchased without further purification. Deionized water was produced in-house and used for the hydrothermal synthesis. Manganese sulfate ($MnSO_4 \cdot H_2O$) and potassium permanganate ($KMnO_4$) used for nanorod synthesis were obtained from Sigma Aldrich.

Hydrothermal Synthesis of α-MnO_2 Nanorods. The α-MnO_2 nanorods were produced in-house by adopting a hydrothermal process reported in literature.[54] Typically, 0.21 g of $KMnO_4$ and 0.49 g of $MnSO_4 \cdot H_2O$ were dissolved in 40 mL deionized water and magnetically stirred for about 20 min to form a homogeneous solution. Then, the solution was transferred into a Teflon-lined stainless steel autoclave and kept at 160 °C for 12 h. The product was collected by centrifugation, washed with DI water, and then dried at 60 °C for 8 h.

Material Characterization. The as-synthesized nanorods and the supercapacitor electrodes prepared by HVEPD were observed using the Hitachi S-4700 FESEM. Powder X-ray diffraction patterns of the α-MnO_2 nanorods were recorded using a Scintag XDS-2000 powder diffractometer with $Cu_{k\alpha}$ radiation (λ = 1.5418 Å). The readings were taken with an operating voltage and current of 40 kV and 40 mA respectively and the 2θ range was set as 10−70° in steps of 0.02° with a count time of 2s.

High Voltage Electrophoretic Deposition. Stable dispersions of as-synthesized α-MnO_2 nanorods (0.01 mg/mL) in isopropyl alcohol (IPA) were prepared by sonicating their mixture for 20 min using a probe sonicator (Sonics and Materials Inc., Connecticut). Precursor salts, $Mg(NO_3)_2 \cdot 6H_2O$ (0.005 mg/mL) and $NiCl_2 \cdot 6H_2O$ (0.0075 mg/mL) (Fisher Scientific, Pennsylvania), were then added to their respective α-MnO_2 nanorod dispersions and sonicated for an additional 15 min. The concentrations of the nanorods were determined from control experiments to maximize deposition density while avoiding bundle formation during HVEPD. The salt concentrations were chosen as the minimal value that the nanorods can receive sufficient positive charges and a uniform holding layer can be formed by the electroplating co-occurring with HVEPD. The dispersions were found stable for at least a couple of weeks. Small, rigid stainless steel (SS) electrodes (McMaster, Illinois) with an exposed area of 2.00 × 2.54 cm^2 were used in the electrophoretic cell with an electrode gap of 10 mm controlled by a spacer. Care was taken to ensure that the electrodes were parallel to each other. A high voltage power source (Stanford Research Systems, California) provided the high voltages needed for HVEPD. The weight of the deposit was measured using a micro balance (Adam Equipment Inc., Connecticut) as 0.08 mg/cm^2. About 10 samples were measured to obtain an accurate average value for the weight of the deposit. HVEPD for the α-MnO_2 nanorods with the Ni holding layer was also conducted on pretreated stainless steel substrates to further reduce contact resistance. A standard Wood's strike was used as pretreatment of the SS substrate to remove its oxide layer and coat a thin layer of nickel. Wood's strike was conducted on the SS electrodes with a nickel counter electrode. The two electrodes were placed in parallel and kept 10 mm away from each other in an electrochemical cell. A current density of around 200 A/m^2 is then applied in the wood's strike solution with 240 g/L of $NiCl_2 \cdot 6H_2O$ and 125 mL/L of HCL.

Electrochemical Characterization. A two-electrode Swagelok cell was used to characterize the redox capacitor electrodes using an electrochemical workstation (Princeton Applied Research, Tennessee). The Swagelok cell was constructed by placing two HVEPD samples in parallel to each other with a filter paper (Whatman, New Jersey) as the separator and 0.1 M Na_2SO_4 as

the electrolyte. The electrolyte was purged with nitrogen before testing. Cyclic voltammetry was conducted within a voltage window of −0.2 − 0.8 V at different scan rates to check the distortion in the shape of the curves at high cycling rates. Galvanostatic charge−discharge testing was conducted within a voltage window of 0−1 V at different current densities to estimate the capacitance and its retention at high cycling rates. Two thousand cycles were run to check the capacitance retention over charge−discharge cycles. Electrochemical impedance spectroscopy was conducted with a 0 V DC bias using a small AC excitation of 10 mV from 10 mHz to 100 kHz.

Continuous HVEPD. The continuous HVEPD setup shown in Figure 2 was used for the deposition of aligned α-MnO_2 nanorods on a long, flexible strip. A 2.54 cm wide, ∼13 μm thick flexible SS strip (McMaster, Illinois) was mounted on the nonconductive rollers and fed at a speed of 5.08 cm/min using a DC motor (McMaster, Illinois). The feed speed of the strip was determined so that any particular point on it can get a deposition time of 30 s, the deposition time for a single layer of densely aligned nanoforest found with the small, rigid samples. Before HVEPD, a continuous Wood's strike was first conducted on the flexible SS sheet, and followed by washing and drying under room temperature. Continuous HVEPD was then conducted on the long strip of pretreated SS sheet. The deposition chamber was first filled with 100 mL of HVEPD dispersion. A multichannel peristaltic pump (Thermo Scientific FH100M, Illinois) was used to continuously replenish the HVEPD dispersion to keep the concentration and volume constant. The pump was set to obtain an inlet and outlet pumping rate of 8 mL/min. The stock dispersion used to replenish the HVEPD bath had a α-MnO_2 nanorod concentration of 0.048 mg/mL and a Ni precursor salt concentration of 0.02 mg/mL. The current was recorded during the continuous HVEPD using a digital multimeter (Universal Enterprises Inc., Orlando) to check for any variations and possible process errors. The deposited long strip was then dried at room temperature. Parts of the long strip with aligned nanoforest were cut and used for FESEM visualization and electrochemical testing.

Conflict of Interest: The authors declare no competing financial interest.

Acknowledgment. This material is based upon work supported by the National Science Foundation under Grant No. 1130651. Any opinions, findings, and conclusions or recommendations expressed in this material are those of the authors and do not necessarily reflect the views of the National Science Foundation.

Supporting Information Available: S1: Cyclic voltammetry. S2: Electrochemical impedance spectroscopy. S3: EDX mapping of as-deposited MnO_2 nanorods. This material is available free of charge *via* the Internet at http://pubs.acs.org.

REFERENCES AND NOTES

1. Camara, M. B.; Gualous, H.; Gustin, F.; Berthon, A. Design and New Control of DC/DC Converters to Share Energy Between Supercapacitors and Batteries in Hybrid Vehicles. *IEEE Trans. Veh. Technol.* **2008**, *57*, 2721–2735.
2. Kuperman, A.; Aharon, I. Battery−Ultracapacitor Hybrids for Pulsed Current Loads: A Review. *Renewable Sustainable Energy Rev.* **2011**, *15*, 981–992.
3. Yoda, S.; Ishihara, K. The Advent of Battery-Based Societies and the Global Environment in the 21st Century. *J. Power Sources* **1999**, *81−82*, 162–169.
4. Kötz, R.; Carlen, M. Principles and Applications of Electrochemical Capacitors. *Electrochim. Acta* **2000**, *45*, 2483–2498.
5. Sarangapani, S.; Tilak, B. V.; Chen, C. P. Materials for Electrochemical Capacitors. *J. Electrochem. Soc.* **1996**, *143*, 3791–3799.
6. Reddy, R. N.; Reddy, R. G. Synthesis and Electrochemical Characterization of Amorphous MnO_2 Electrochemical Capacitor Electrode Material. *J. Power Sources* **2004**, *132*, 315–320.
7. Burke, A. Ultracapacitors: Why, How, and Where Is the Technology. *J. Power Sources* **2000**, *91*, 37–50.
8. An, K. H.; Kim, W. S.; Park, Y. S.; Moon, J. M.; Bae, D. J.; Lim, S. C.; Lee, Y. S.; Lee, Y. H. Electrochemical Properties of High-Power Supercapacitors Using Single-Walled Carbon Nanotube Electrodes. *Adv. Funct. Mater.* **2001**, *11*, 387–392.
9. Chunsheng, D.; Yeh, J.; Pan, N. High Power Density Supercapacitors Using Locally Aligned Carbon Nanotube Electrodes. *Nanotechnology* **2005**, *16*, 350.
10. Frackowiak, E.; Béguin, F. Carbon Materials for the Electrochemical Storage of Energy in Capacitors. *Carbon* **2001**, *39*, 937–950.
11. Malinauskas, A.; Malinauskienė, J.; Ramanavičius, A. Conducting Polymer-Based Nanostructurized Materials: Electrochemical Aspects. *Nanotechnology* **2005**, *16*, R51.
12. Peng, C.; Jin, J.; Chen, G. Z. A Comparative Study on Electrochemical Co-Deposition and Capacitance of Composite Films of Conducting Polymers and Carbon Nanotubes. *Electrochim. Acta* **2007**, *53*, 525–537.
13. Sugimoto, W.; Yokoshima, K.; Murakami, Y.; Takasu, Y. Charge Storage Mechanism of Nanostructured Anhydrous and Hydrous Ruthenium-Based Oxides. *Electrochim. Acta* **2006**, *52*, 1742–1748.
14. Young Rack, A.; Song, M. Y.; Jo, S. M.; Park, C. R.; Kim, D. Y. Electrochemical Capacitors Based on Electrodeposited Ruthenium Oxide on Nanofibre Substrates. *Nanotechnology* **2006**, *17*, 2865.
15. Jiang, J.; Kucernak, A. Electrochemical Supercapacitor Material Based on Manganese Oxide: Preparation and Characterization. *Electrochim. Acta* **2002**, *47*, 2381–2386.
16. Nelson, P. A.; Owen, J. R. A High-Performance Supercapacitor/Battery Hybrid Incorporating Templated Mesoporous Electrodes. *J. Electrochem. Soc.* **2003**, *150*, A1313–A1317.
17. Hibino, M.; Abe, K.; Mochizuki, M.; Miyayama, M. Amorphous Titanium Oxide Electrode for High-Rate Discharge and Charge. *J. Power Sources* **2004**, *126*, 139–143.
18. Hu, C.-C.; Huang, C.-M.; Chang, K.-H. Anodic Deposition of Porous Vanadium Oxide Network with High Power Characteristics for Pseudocapacitors. *J. Power Sources* **2008**, *185*, 1594–1597.
19. Wang, G.; Zhang, L.; Zhang, J. A Review of Electrode Materials for Electrochemical Supercapacitors. *Chem. Soc. Rev.* **2012**, *41*, 797–828.
20. Xu, C.; Kang, F.; Li, B.; Du, H. Recent Progress on Manganese Dioxide Based Supercapacitors. *J. Mater. Res.* **2010**, *25*, 1421–1432.
21. Devaraj, S.; Munichandraiah, N. Effect of Crystallographic Structure of MnO_2 on Its Electrochemical Capacitance Properties. *J. Phys. Chem. C* **2008**, *112*, 4406–4417.
22. Jeyagowry, T. S.; Jian, D.; Gan Geok, J.; Effendi, W.; Low Qui Hui, E. Template-Free Low Temperature Hydrothermal Synthesis and Characterization of Rod-Shaped Manganese Oxyhydroxides and Manganese Oxides. *Nanotechnology* **2007**, *18*, 025601.
23. Arico, A. S.; Bruce, P.; Scrosati, B.; Tarascon, J.-M.; van Schalkwijk, W. Nanostructured Materials for Advanced Energy Conversion and Storage Devices. *Nat. Mater.* **2005**, *4*, 366–377.
24. Liu, J.; Cao, G.; Yang, Z.; Wang, D.; Dubois, D.; Graff, X. Z. G. L.; Pederson, L. R.; Zhang, J.-G. Oriented Nanostructures for Energy Conversion and Storage. *ChemSusChem* **2008**, *1*, 676–697.
25. Dai, L.; Patil, A.; Gong, X.; Guo, Z.; Liu, L.; Liu, Y.; Zhu, D. Aligned Nanotubes. *ChemPhysChem* **2003**, *4*, 1150–1169.
26. Jiang, Y. Q.; Zhou, Q.; Lin, L. Planar MEMS Supercapacitor Using Carbon Nanotube Forests. *IEEE Int. Conf. Micro Electro Mech. Syst., Tech. Dig., 22nd* **2009**, 587–590.
27. In, H. J.; Kumar, S.; Shao-Horn, Y.; Barbastathis, G. Origami Fabrication of Nanostructured, Three-Dimensional Devices: Electrochemical Capacitors with Carbon Electrodes. *Appl. Phys. Lett.* **2006**, *88*, 083104–3.
28. Zhang, H.; Cao, G.; Wang, Z.; Yang, Y.; Shi, Z.; Gu, Z. Growth of Manganese Oxide Nanoflowers on Vertically-Aligned Carbon Nanotube Arrays for High-Rate Electrochemical Capacitive Energy Storage. *Nano Lett.* **2008**, *8*, 2664–2668.

29. Coll, B. F.; Dean, K. A.; O'Rourke, S. M.; Stainer, M.; Subrahmanyan, R.; Talin, A. A. FED Cathode Structure Using Electrophoretic Deposition and Method of Fabrication. U.S. Patent No. 6902658 B2, 2005.
30. Jin, Y. W.; Jung, J. E.; Park, Y. J.; Choi, J. H.; Jung, D. S.; Lee, H. W.; Park, S. H.; Lee, N. S.; Kim, J. M.; Ko, T. Y.; et al. Triode-Type Field Emission Array Using Carbon Nanotubes and a Conducting Polymer Composite Prepared by Electrochemical Polymerization. *J. Appl. Phys.* **2002**, *92*, 1065–1068.
31. Kim, S.-K.; Lee, H.; Tanaka, H.; Weiss, P. S. Vertical Alignment of Single-Walled Carbon Nanotube Films Formed by Electrophoretic Deposition. *Langmuir* **2008**, *24*, 12936–12942.
32. Nakayama, Y.; Akita, S. Field-Emission Device with Carbon Nanotubes for a Flat Panel Display. *Synth. Methods* **2001**, *117*, 207–210.
33. Quale, S. L.; Talbot, J. B. Electrophoretic Deposition of Substrate-Normal-Oriented Single-Walled Carbon Nanotube Structures. *J. Electrochem. Soc.* **2007**, *154*, K25–K28.
34. Chen, X. Q.; Saito, T.; Yamada, H.; Matsushige, K. Aligning Single-Wall Carbon Nanotubes with an Alternating-Current Electric Field. *Appl. Phys. Lett.* **2001**, *78*, 3714–3716.
35. Yamamoto, K.; Akita, S.; Nakayama, Y. Orientation and Purification of Carbon Nanotubes Using ac Electrophoresis. *J. Phys. D: Appl. Phys.* **1998**, *31*, L34–L36.
36. Moscatello, J.; Kayastha, V.; Ulmen, B.; Pandey, A.; Wu, S.; Singh, A.; Yap, Y. K. Surfactant-Free Dielectrophoretic Deposition of Multi-Walled Carbon Nanotubes with Tunable Deposition Density. *Carbon* **2010**, *48*, 3559–3569.
37. Ahmed, W.; Kooij, E. S.; van Silfhout, A.; Poelsema, B. Quantitative Analysis of Gold Nanorod Alignment after Electric Field-Assisted Deposition. *Nano Lett.* **2009**, *9*, 3786–3794.
38. Toupin, M.; Brousse, T.; Bélanger, D. Charge Storage Mechanism of MnO_2 Electrode Used in Aqueous Electrochemical Capacitor. *Chem. Mater.* **2004**, *16*, 3184–3190.
39. Kim, H.; Popov, B. N. Synthesis and Characterization of MnO_2-Based Mixed Oxides as Supercapacitors. *J. Electrochem. Soc.* **2003**, *150*, D56–D62.
40. Pang, S.-C.; Anderson, M. A. Novel Electrode Materials for Electrochemical Capacitors: Part II. Material Characterization of Sol-Gel-Derived and Electrodeposited Manganese Dioxide Thin Films. *J. Mater. Res.* **2000**, *15*, 2096–2106.
41. Wang, X.; Wang, X.; Huang, W.; Sebastian, P. J.; Gamboa, S. Sol-Gel Template Synthesis of Highly Ordered MnO_2 Nanowire Arrays. *J. Power Sources* **2005**, *140*, 211–215.
42. Xia, H.; Feng, J.; Wang, H.; Lai, M. O.; Lu, L. MnO_2 Nanotube and Nanowire Arrays by Electrochemical Deposition for Supercapacitors. *J. Power Sources* **2010**, *195*, 4410–4413.
43. Xu, C.-L.; Bao, S.-J.; Kong, L.-B.; Li, H.; Li, H.-L. Highly Ordered MnO_2 Nanowire Array Thin Films on Ti/Si Substrate as an Electrode for Electrochemical Capacitor. *J. Solid State Chem.* **2006**, *179*, 1351–1355.
44. Babakhani, B.; Ivey, D. G. Anodic Deposition of Manganese Oxide Electrodes with Rod-Like Structures for Application as Electrochemical Capacitors. *J. Power Sources* **2010**, *195*, 2110–2117.
45. Xu, M.; Kong, L.; Zhou, W.; Li, H. Hydrothermal Synthesis and Pseudocapacitance Properties of α-MnO_2 Hollow Spheres and Hollow Urchins. *J. Phys. Chem. C* **2007**, *111*, 19141–19147.
46. Subramanian, V.; Zhu, H.; Vajtai, R.; Ajayan, P. M.; Wei, B. Hydrothermal Synthesis and Pseudocapacitance Properties of MnO_2 Nanostructures. *J. Phys. Chem B* **2005**, *109*, 20207–20214.
47. Chen, X.; Li, X.; Jiang, Y.; Shi, C.; Li, X. Rational Synthesis of α-MnO_2 and γ-Mn_2O_3 Nanowires with the Electrochemical Characterization of α-MnO_2 Nanowires for Supercapacitor. *Solid State Commun.* **2005**, *136*, 94–96.
48. Yang, Y.; Xiao, L.; Zhao, Y.; Wang, F. Hydrothermal Synthesis and Electrochemical Characterization of α-MnO_2 Nanorods as Cathode Material for Lithium Batteries. *Int. J. Electrochem. Sci.* **2008**, *3*, 67–74.
49. Subramanian, V.; Zhu, H.; Wei, B. Nanostructured MnO_2: Hydrothermal Synthesis and Electrochemical Properties as a Supercapacitor Electrode Material. *J. Power Sources* **2006**, *159*, 361–364.
50. Brousse, T.; Toupin, M.; Dugas, R.; Athouel, L.; Crosnier, O.; Belanger, D. Crystalline MnO_2 as Possible Alternatives to Amorphous Compounds in Electrochemical Supercapacitors. *J. Electrochem. Soc.* **2006**, *153*, A2171–A2180.
51. Talapatra, S.; Kar, S.; Pal, S. K.; Vajtai, R.; Ci, L.; Victor, P.; Shaijumon, M. M.; Kaur, S.; Nalamasu, O.; Ajayan, P. M. Direct Growth of Aligned Carbon Nanotubes on Bulk Metals. *Nat. Nanotechnol.* **2006**, *1*, 112–116.
52. Santhanagopalan, S.; Teng, F.; Meng, D. D. High-Voltage Electrophoretic Deposition for Vertically Aligned Forests of One-Dimensional Nanoparticles. *Langmuir* **2010**, *27*, 561–569.
53. Boccaccini, A. R.; Cho, J.; Roether, J. A.; Thomas, B. J. C.; Jane Minay, E.; Shaffer, M. S. P. Electrophoretic Deposition of Carbon Nanotubes. *Carbon* **2006**, *44*, 3149–3160.
54. Wang, X.; Li, Y. Synthesis and Formation Mechanism of Manganese Dioxide Nanowires/Nanorods. *Chem.—Eur. J.* **2003**, *9*, 300–306.
55. Liang, S.; Teng, F.; Bulgan, G.; Zong, R.; Zhu, Y. Effect of Phase Structure of MnO_2 Nanorod Catalyst on the Activity for CO Oxidation. *J. Phys. Chem. C* **2008**, *112*, 5307–5315.
56. Cho, J.; Konopka, K.; Rozniatowski, K.; García-Lecina, E.; Shaffer, M. S. P.; Boccaccini, A. R. Characterisation of Carbon Nanotube Films Deposited by Electrophoretic Deposition. *Carbon* **2009**, *47*, 58–67.
57. Han, S. P.; Yang, S.-M. Orientation Distribution and Electrophoretic Motions of Rod-Like Particles in a Capillary. *J. Colloid Interface Sci.* **1996**, *177*, 132–142.
58. Kamat, P. V.; Thomas, K. G.; Barazzouk, S.; Girishkumar, G.; Vinodgopal, K.; Meisel, D. Self-Assembled Linear Bundles of Single Wall Carbon Nanotubes and Their Alignment and Deposition as a Film in a dc Field. *J. Am. Chem. Soc.* **2004**, *126*, 10757–10762.
59. Santhanagopalan, S.; Teng, F.; Meng, D. D. IC-Compatible Deposition of Vertically-Aligned CNT Forests for Micro-Supercapacitors. *Power MEMS Int. Workshop, Tech. Dig., 9th* **2009**, 593–596.
60. Dini, J. W. Adhesion. In *Electrodeposition: The Materials Science of Coatings and Substrates*; Bunshah, R. F., McGuire, G. E., Rossnagel, S. M., Eds.; Noyes Publications: Saddle River, NJ, 1993; pp 59−63.
61. Stoller, M. D.; Ruoff, R. S. Best Practice Methods for Determining an Electrode Material's Performance for Ultracapacitors. *Energy Environ. Sci.* **2010**, *3*, 1294–1301.
62. Rajendra Prasad, K.; Miura, N. Electrochemically Synthesized MnO_2-Based Mixed Oxides for High Performance Redox Supercapacitors. *Electrochem. Commun.* **2004**, *6*, 1004–1008.
63. Ye, Z. G.; Zhou, X. L.; Meng, H. M.; Hua, X. Z.; Dong, Y. H.; Zou, A. H. The Electrochemical Characterization of Electrochemically Synthesized MnO_2-Based Mixed Oxides for Supercapacitor Applications. *Adv. Mat. Res.* **2011**, *287−290*, 1290–1298.
64. Lei, Y.; Daffos, B.; Taberna, P. L.; Simon, P.; Favier, F. MnO_2-Coated Ni Nanorods: Enhanced High Rate Behavior in Pseudo-Capacitive Supercapacitor. *Electrochim. Acta* **2010**, *55*, 7454–7459.
65. Wei, W.; Cui, X.; Chen, W.; Ivey, D. G. Electrochemical Cyclability Mechanism for MnO_2 Electrodes Utilized as Electrochemical Supercapacitors. *J. Power Sources* **2009**, *186*, 543–550.
66. Yu, G.; Hu, L.; Vosgueritchian, M.; Wang, H.; Xie, X.; McDonough, J. R.; Cui, X.; Cui, Y.; Bao, Z. Solution-Processed Graphene/MnO_2 Nanostructured Textiles for High-Performance Electrochemical Capacitors. *Nano Lett.* **2011**, *11*, 2905–2911.
67. Chen, S.; Zhu, J.; Wu, X.; Han, Q.; Wang, X. Graphene Oxide−MnO_2 Nanocomposites for Supercapacitors. *ACS Nano* **2010**, *4*, 2822–2830.
68. Wu, Z.-S.; Ren, W.; Wang, D.-W.; Li, F.; Liu, B.; Cheng, H.-M. High-Energy MnO_2 Nanowire/Graphene and Graphene Asymmetric Electrochemical Capacitors. *ACS Nano* **2010**, *4*, 5835–5842.

69. Hu, L.; Chen, W.; Xie, X.; Liu, N.; Yang, Y.; Wu, H.; Yao, Y.; Pasta, M.; Alshareef, H. N.; Cui, Y. Symmetrical MnO_2–Carbon Nanotube–Textile Nanostructures for Wearable Pseudocapacitors with High Mass Loading. *ACS Nano* **2011**, *5*, 8904–8913.
70. Yuan, L.; Lu, X.-H.; Xiao, X.; Zhai, T.; Dai, J.; Zhang, F.; Hu, B.; Wang, X.; Gong, L.; Chen, J.; et al. Flexible Solid-State Supercapacitors Based on Carbon Nanoparticles/MnO_2 Nanorods Hybrid Structure. *ACS Nano* **2011**, *6*, 656–661.
71. Masarapu, C.; Zeng, H. F.; Hung, K. H.; Wei, B. Effect of Temperature on the Capacitance of Carbon Nanotube Supercapacitors. *ACS Nano* **2009**, *3*, 2199–2206.
72. Hu, C.-C.; Chang, K.-H.; Lin, M.-C.; Wu, Y.-T. Design and Tailoring of the Nanotubular Arrayed Architecture of Hydrous RuO_2 for Next Generation Supercapacitors. *Nano Lett.* **2006**, *6*, 2690–2695.
73. Yu, Z.; Zinger, D.; Bose, A. An Innovative Optimal Power Allocation Strategy for Fuel Cell, Battery and Supercapacitor Hybrid Electric Vehicle. *J. Power Sources* **2011**, *196*, 2351–2359.
74. Thounthong, P.; Raël, S.; Davat, B. Energy Management of Fuel Cell/Battery/Supercapacitor Hybrid Power Source for Vehicle Applications. *J. Power Sources* **2009**, *193*, 376–385.
75. Dan, B.; Irvin, G. C.; Pasquali, M. Continuous and Scalable Fabrication of Transparent Conducting Carbon Nanotube Films. *ACS Nano* **2009**, *3*, 835–843.
76. Kleinstreuer, C. Fundamental Equations and Solutions. In *Modern Fluid Dynamics: Basic Theory and Selected Applications in Macro- and Micro-Fluidics*; Moreau, R., Madylam, Eds.; Springer: New York, 2010; Vol. 87; pp 69–73.
77. Santhanagopalan, S.; Balram, A.; Lucas, E.; Marcano, F.; Meng, D. D. High Voltage Electrophoretic Deposition of Aligned Nanoforests for Scalable Nanomanufacturing of Electrochemical Energy Storage Devices. *Key Eng. Mater.* **2012**, *507*, 67–72.